

# Extra-heating mechanism in Doppler cooling experiments

Thierry Chanelière, Jean-Louis Meunier, Robin Kaiser, Christian Miniatura, and David Wilkowski

*Institut non linéaire de Nice, Unité Mixte de Recherche 6618 du Centre National de la Recherche Scientifique, 1361 route de Lucioles, F-06560 Valbonne, France*

Received December 23, 2004; accepted February 24, 2005

We experimentally and theoretically investigate laser cooling of strontium-88 atoms in one-dimensional optical molasses. In our case, since the optical cooling dipole transition involves a  $J_g=0$  ground state, no Sisyphus-type mechanisms can occur. We are thus able to test quantitatively the predictions of the Doppler cooling theory. We have found, in agreement with other similar experiments, that the measured temperatures are systematically larger than the theoretical predictions. We quantitatively interpret this discrepancy by taking into consideration the extra-heating mechanism induced by transverse spatial intensity fluctuations of the optical molasses. Experimental data are in good agreement with Monte Carlo simulations of our theoretical model. We thus confirm the important role played by intensity fluctuations in the dynamics of cooling and for the steady-state regime. © 2005 Optical Society of America  
OCIS code: 140.3320.

## 1. INTRODUCTION

Initiated in the mid-seventies, laser cooling, trapping, and manipulation of atoms rapidly became a successful field of research,<sup>1</sup> culminating 20 years later with the observation of Bose–Einstein condensation of alkaline atoms.<sup>2,3</sup> This success story began with the seminal Doppler cooling theory that was designed for two-level systems.<sup>4,5</sup> However, the first reliable tests of the Doppler theory could be performed only at the end of the eighties. As it turned out, the measured temperatures in the experiments were well below the predicted Doppler values.<sup>6</sup> These surprising results indicated that another, much more efficient, cooling mechanism was at work in the experiments. This mechanism, now known as Sisyphus cooling, was identified soon after.<sup>7,8</sup> The key point was to understand that internal ground-state degeneracies were opening the way to a new cooling mechanism based on optical pumping in the presence of polarization gradients. This cooling mechanism is now the basic ingredient for most experiments in the field and thus gave the Doppler theory a more academic status.

Recent laser technological advances, however, opened the way to cooling and trapping experiments with earth-alkaline and rare-earth atoms [calcium (Ca), magnesium (Mg), strontium (Sr), and Ytterbium (Yb)]. As these atoms exhibit a zero-spin ground state, Sisyphus cooling is absent. Interest in testing the Doppler theory to gain better control on achievable temperatures has thus been renewed. To our knowledge, all experiments on laser cooling of these atoms<sup>9–13</sup> always reported much larger temperatures than the Doppler theory prediction. This is a strong clue in favor of an extra-heating mechanism still to be clearly identified. Approaching the Doppler limit in magneto-optical traps (MOTs) operating with earth-alkaline atoms seems a challenge, and a better understanding of this heating mechanism is required for future experimental improvements. To our knowledge, only one

explanation has been published to understand these high temperatures.<sup>14</sup> The argumentation is based on heating induced by inelastic collisions. However, as the authors themselves show, this heating mechanism sets in only for atomic densities much higher than for those measured in typical MOTs ( $10^9$ – $10^{11}$  atoms/cm<sup>3</sup>). For this reason, their explanation fails to understand the results presented in that paper and also in all previously cited publications.

Heating mechanisms depending on the density or the number of atoms or both in the cold MOT cloud are well known even for degenerate ground-state atoms.<sup>15</sup> They essentially rely on reabsorption of scattered photons in the cold MOT.<sup>16</sup> This situation is encountered as soon as light multiple scattering sets in, i.e., when the light-scattering mean free path  $\ell$  is comparable with the MOT size  $L$ . Similar multiatom and multiphoton effects certainly also exist with earth-alkaline MOTs, but they can be made negligible by one's working at low densities ( $n \approx 2.5 \times 10^9$  atoms/cm<sup>3</sup>) and at low optical thickness ( $b = L/\ell \approx 0.3$  at resonance).

Strictly speaking, Doppler theory can also be tested with degenerate atoms, provided that a suitable molasses polarization configuration is chosen.<sup>17</sup> Indeed, for one-dimensional (1D) cooling with parallel polarizations ( $\sigma^+ - \sigma^+$  or  $\pi - \pi$  configurations), no Sisyphus cooling can occur. However, even in this case, the authors found unusually high temperatures. They suggested that this discrepancy was due to a molasses intensity imbalance, leading to a local drift of the atomic average velocity in the cloud. We agree with this explanation, as we will show in detail in this paper.

We have performed specific temperature measurements on <sup>88</sup>Sr (Sr in short hereafter) in a 1D cooling configuration. This is the ideal situation to test the Doppler theory for two reasons. First, we induce cooling on a  $J_g = 0 \rightarrow J_e = 1$  atomic optical transition. Second, two-

dimensional or three-dimensional Doppler cooling would be more difficult to analyze quantitatively. Indeed, interference between the six laser MOT beams can induce light-shift modulations, leading to modifications of the usual friction and diffusion coefficients.<sup>18</sup> These spurious effects do not exist in the 1D configuration with mutual orthogonal polarized counterpropagating laser beams. The new important ingredient here is that we incorporate in the original Doppler theory the effect of transverse spatial intensity fluctuations of the laser molasses profiles.

The paper is organized as follows. After some details about the experimental procedure, we compare velocity dispersion measurements with the Doppler theory predictions (Section 2). We have found temperatures ten times larger than predicted. Indeed, at a laser detuning  $\delta = -\Gamma/2$ , we have measured a velocity dispersion  $\sigma_v = 0.7 \pm 0.2$  m/s ( $T \approx 5$  mK), whereas the Doppler theory predicts  $\sigma_v = 0.23$  m/s ( $T \approx 0.5$  mK). In Section 3 we will show, on general arguments, why the molasses transverse intensity fluctuations heat the cold cloud. We then derive an analytical model valid in two limiting cases: when the transverse distance  $L_\perp$  traveled by an atom during the longitudinal velocity damping time is much shorter or much longer than the transverse correlation length  $\xi_s$  of the molasses intensity fluctuations. As expected, these two different limits give rise to different final velocity distributions. In Subsection 3.D, we will compare our results with a Monte Carlo (MC) simulation. Most of our experimental data correspond to  $L_\perp \ll \xi_s$ . In this case, the dynamics of the velocity distribution shows an unusual behavior. The velocity dispersion  $\sigma_v$  is first reduced by the friction force and then increases after a time scale related to  $\xi_s$  (Section 4). This specific behavior confirms the dominant role played by the transverse intensity fluctuations in 1D cooling with a  $J_g=0 \rightarrow J_e=1$  transition.

## 2. EXPERIMENTAL RESULTS

### A. Magneto-Optical Trap

The cold Sr cloud is produced in a MOT. The  $J_g=0 \rightarrow J_e=1$  dipole transition under consideration is the optical atomic line  $^1S_0 - ^1P_1$  at  $\lambda = 461$  nm. The excited-state natural linewidth is  $\Gamma/2\pi = 32$  MHz, and the corresponding saturation intensity is  $I_s = 42.5$  mW/cm<sup>2</sup>. First, an effusive Sr beam is extracted from a 500 °C oven. Then a 27 cm long Zeeman slower reduces the Sr longitudinal velocity within the velocity capture range of the MOT ( $\sim 50$  m/s). The Zeeman slower, MOT, and probe laser beams operate at 461 nm and are generated from the same frequency-doubled source detailed in Ref. 19. Briefly, a single-mode grating-stabilized diode laser and a tapered amplifier are used in a master-slave configuration to produce 500 mW of light at 922 nm. This infrared light is then frequency doubled in a semimonolithic standing-wave cavity with an intracavity KNbO<sub>3</sub> nonlinear crystal. The cavity is resonant for the infrared light, and the second harmonic exits through a dichroic mirror, providing 150 mW of tunable single-mode light, which is then frequency locked on the 461 nm Sr line in a heat pipe. We use acousto-optic modulators for subsequent amplitude and frequency variations. The MOT is made of six independent trapping beams. Each beam carries an inten-

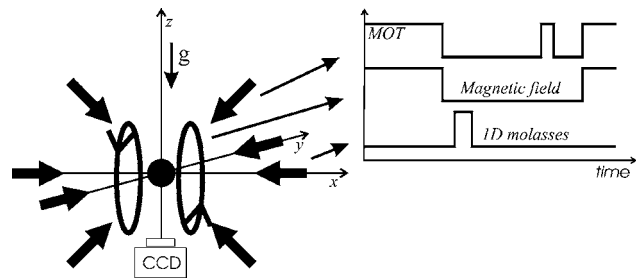


Fig. 1. Schematic drawing of our setup and of the time sequence used in the experiment. The six independent MOT laser beams are along the  $x$  axis and in the vertical plane ( $yz$ ) at  $45^\circ$  with respect to the  $z$  axis. The 1D cooling beams contrapropagate along the  $y$  axis. The recorded CCD images correspond to the cloud fluorescence signal integrated over  $z$ .

sity of  $5.2$  mW/cm<sup>2</sup>, and each beam waist is 8 mm. The trapping beams are red detuned by  $\delta = -\Gamma$  with respect to the atomic resonance. Two anti-Helmoltz coils generate a 70 G/cm magnetic field gradient to trap the atoms. The number of trapped atoms, as deduced from fluorescence measurements, is  $N \approx 2.5 \times 10^6$ . The (Gaussian-shaped) cloud dispersion is roughly 0.6 mm. The velocity dispersion of atoms in the MOT is typically  $\Delta v \sim 1$  m/s. Technical details about temperature measurements are given in Subsection 2.B.

### B. One-Dimensional Cooling and Time-of-Flight Measurements

In addition to the previously discussed experimental setup (MOT and Zeeman slower), two additional counterpropagating laser beams are used to perform a 1D molasses (see Fig. 1). These 1D cooling beams are located in the horizontal plane. Some quarter-wave and half-wave plates are used to fix the relative polarizations of the two counterpropagating laser beams. An acousto-optical modulator in a double-pass configuration is used to adjust the laser frequency from resonance down to  $-\Gamma$ . The same acousto-optical modulator is used to control the laser intensity up to  $I_s$ . The beam waist is 3.5 mm at the cold cloud position, thus much bigger than the MOT size.

The time sequence of the experiment is generated by a personal computer with digital output ports dedicated to this task. An internal clock updates and synchronizes the digital output ports every  $10 \mu\text{s}$ . This elementary time step is short enough for our purposes. The digital output ports are connected to switches that turn on and off the laser beams (rising and falling times shorter than  $1 \mu\text{s}$ ), the magnetic field (rising time of a few milliseconds and falling time of  $100 \mu\text{s}$ ), and the CCD camera chopper (opening and closing times of  $200 \mu\text{s}$ ). The time sequence is designed as follows: First, the MOT is operated for approximately 20 ms. Then the MOT lasers and magnetic gradient are switched off. The 1D molasses laser beams are then switched on for  $500 \mu\text{s}$ . This cooling time is appropriately chosen: Atoms reach the cooling steady-state regime while, at the same time, the expanding atomic cloud remains smaller than the cooling beams' size. After the 1D cooling sequence, the temperature of the cold cloud is extracted from a time-of-flight (TOF) measurement technique. For this purpose, all the laser beams are switched off, and the cold cloud expands ballistically in

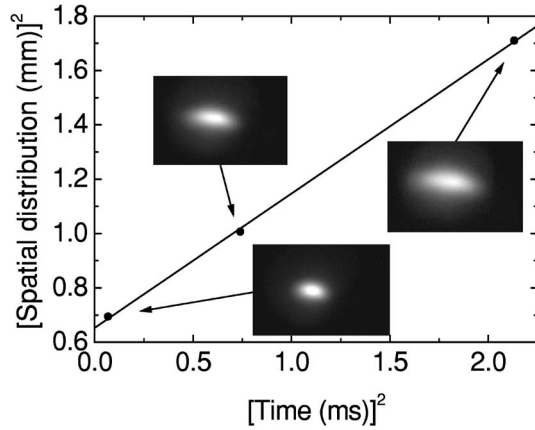


Fig. 2. After the 1D cooling sequence along axis  $y$ , the spatial distribution in the horizontal plane is collected at three ballistic expansion times by the TOF technique. From these images, we extract the velocity dispersion  $\sigma_v$  in the cloud (see text).

the dark. The duration of the dark period is varied from a few 100  $\mu\text{s}$  to 1.5 ms. Then a fluorescence image of the expanding cloud is recorded on the CCD camera by our briefly switching on the MOT beams for 20  $\mu\text{s}$ . The whole time sequence is then repeated as long as necessary to obtain a good signal-to-noise ratio (see Fig. 1).

Figure 2 shows three images of the cloud after different ballistic expansion times. The elliptical shape of the cloud is a signature of the 1D cooling sequence. Indeed, the cooling axis is precisely the small axis of the ellipse. This dimension will be thereafter referenced as the longitudinal axis. In the two other dimensions, thereafter referenced as the transverse axes, the cloud is heated by random spontaneous emission. From these images, we extract the dispersion of the longitudinal spatial distribution of atoms in the cloud, integrated over the transverse directions. Because of the finite size of the image, we cannot have access to the long tail of the spatial distribution. Hence, we truncate all recorded distributions at 2% of their maximum value. Assuming the initial atomic positions and velocities in the MOT to be uncorrelated and centered, one finds that the ballistic time evolution of the spatial dispersion is simply  $\sigma_x^2(t) = \sigma_x^2(0) + \sigma_v^2 t^2$ . The velocity dispersion  $\sigma_v = (\langle v^2 \rangle)^{1/2}$  is then easily extracted from the experimental data. To cross check these measurements, we have also used a different measurement method, namely, a spectroscopic technique. It consists in probing the cold cloud with an ultrastable laser beam tuned on resonance with the  $^1S_0 - ^3P_1$  Sr transition line (note that this is also a  $0 \rightarrow 1$  transition). Because this line is spin forbidden, its frequency width is small (7.5 kHz) and is thus Doppler broadened in the MOT. Hence, we have a direct access to the velocity distribution by measuring the Doppler-induced spectral width. We have checked that these two different techniques give the same results, thereby confirming the validity of the TOF measurements; also, they are easier to handle and, for this reason, routinely used in this experiment for temperature measurements.

### C. Doppler Theory and Results

Doppler theory is based on absorption–fluorescence cycles, which induce a cooling mechanism competing with

a heating mechanism. Cooling is due to a mean friction force  $F = -m\gamma v$  that damps the velocity, and heating is due to a Langevin fluctuating force  $F_v$  (photon noise) giving rise to diffusion with constant  $D$  in velocity space. At equilibrium these processes exactly balance (fluctuation–dissipation theorem), and the Doppler temperature is found to be  $k_B T_D = m\sigma_D^2 = mD/\gamma$ . All experimental data presented in this paper have been obtained in the lin||lin polarization configuration. In this case, analytical expressions for the damping coefficient  $\gamma$  can be found in Ref. 20 and in Ref. 6 for the diffusion constant  $D$ . The analytical expression of the Doppler variance at low laser intensities  $I$  and negative detuning  $\delta$  is then

$$\begin{aligned} \sigma_D^2 &= \frac{D}{\gamma} \approx \frac{7}{20} \frac{\hbar\Gamma}{m} \frac{1 + \Delta^2}{2|\Delta|} \left[ 1 + \frac{2}{7} \frac{11 + \Delta^2}{(1 + \Delta^2)^2} s_0 \right] \\ &= \sigma_0^2(\Delta) [1 + 2\beta(\Delta)s_0]. \end{aligned} \quad (1)$$

Here  $\Delta = 2\delta/\Gamma$  is the laser detuning in units of  $\Gamma/2$ , and  $s_0 = I/I_s$  is the on-resonance saturation parameter. As could have been guessed, the Doppler temperature is related to the only energy scale of the problem, namely, the excited-state energy width  $\hbar\Gamma$ . We thus see that, at low intensities,  $\sigma_D \approx \sigma_0(\Delta)[1 + \beta(\Delta)s_0]$  grows linearly in  $s_0$  with slope  $\beta(\Delta)\sigma_0(\Delta)$  from  $\sigma_0(\Delta)$ . Minimization of  $\sigma_0(\Delta)$  is achieved for  $\Delta = -1$  and gives  $\beta = 3/7$ ,  $\sigma_0 = (7\hbar\Gamma/20m)^{1/2} \approx 0.23$  m/s.

In the strict 1D Doppler theory, the final velocity distribution and the corresponding temperature should depend on the polarization configuration. For example, in the lin||lin polarization channel, photon redistribution processes between the two contrapropagating laser fields can occur, whereas they are forbidden in the lin  $\perp$  lin polarization channel. Hence, the polarization configuration affects both friction and diffusion. We have tested different polarization configurations (lin||lin, lin  $\perp$  lin, and  $\sigma^+ - \sigma^-$ ), but no significative temperature modifications have been found in the parameter range used in this experiment (see below).

Figure 3 shows the experimental variation of the velocity dispersion  $\sigma_v$  as a function of  $\Delta$  at low intensity ( $s_0$

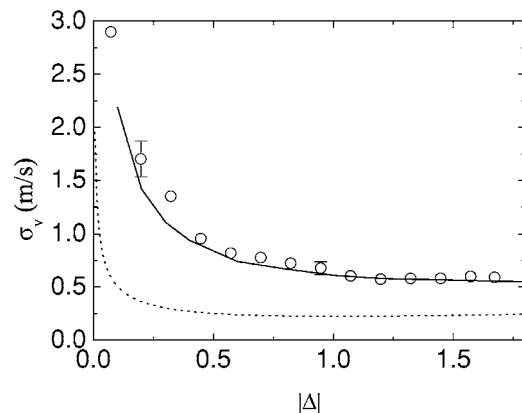


Fig. 3. Velocity dispersion  $\sigma_v$  as a function of  $|\Delta| = 2|\delta|/\Gamma$  for  $s_0 = I/I_s = 0.08$ . The experimental data (circles) are compared with the Doppler prediction (dotted curve) and with the MC simulation (solid curve) at  $r_s = 9\%$  and  $\xi_s = 60$   $\mu\text{m}$  (see Section 3). As one can see, the Doppler theory is completely off, whereas good agreement is obtained with our theoretical model (see text).

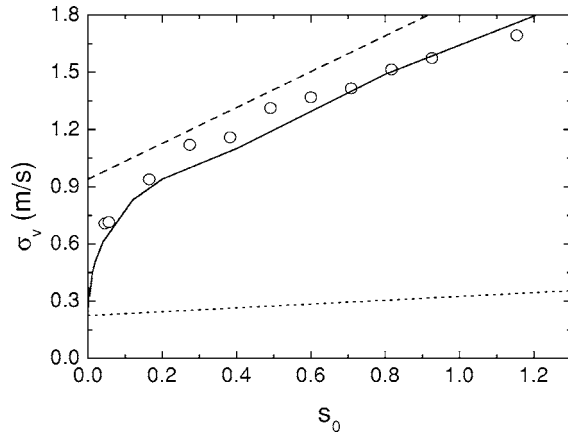


Fig. 4. Velocity dispersion  $\sigma_v$  as a function of the mean saturation parameter  $s_0 = I/I_s$  at  $\Delta = 2\delta/\Gamma = -1$ . The experimental data (circles) are compared with the Doppler prediction (dotted curve) and with the MC simulation (solid curve) at  $r_s = 9\%$  and  $\xi_s = 60 \mu\text{m}$  (see Section 3). Whereas the Doppler theory is completely off, good agreement is found with our theoretical model. The dashed-line prediction corresponds to Eq. (9) (see text).

$= 0.08$ ). The global behavior is the same as the one predicted by the Doppler theory but systematically higher. For example, at  $\Delta = -1$ , we get  $\sigma_v = 0.7 \pm 0.2 \text{ m/s}$  ( $T \approx 5 \text{ mK}$ ), whereas the Doppler theory predicts  $\sigma_v \approx \sigma_0 \approx 0.23 \text{ m/s}$  ( $T \approx 5 \text{ mK}$ ). The mismatch is even more pronounced at small detuning and tends to be reduced at high detuning. Figure 4, obtained at  $\Delta = -1$ , shows a strong linear increase of  $\sigma_v$  as a function of  $s_0$ . The measured slope is  $0.9 \text{ m/s}$ , whereas the Doppler theory predicts only  $0.1 \text{ m/s}$ .

The on-resonance optical thickness corresponding to the data in Figs. 3 and 4 is typically  $b \approx 0.3$  when the experimental sequence starts. At the end of the sequence, because the atomic cloud expands,  $b \approx 0.15$ . These optical thicknesses are not sufficiently low to discard multiple-scattering effects (this would require  $b \ll 1$ ). The role of multiple scattering of light is twofold. First, it induces photon reabsorption, leading to an average repulsion force and heating. However, at  $b \approx 0.3$ , heating, as observed in Ref. 15, can here be neglected. Second, it implies beam attenuation (Lambert–Beer law). This means that the average optical force is weaker for atoms located deep in the cloud, and we get, as a net effect, an average compression force. In a MOT, these compression and repulsion forces are equilibrated by the trapping force.<sup>21</sup> This is not the case in optical molasses. In a 1D molasses, the compression force is expected to dominate over the repulsion force induced by photon reabsorption, at least at moderate optical thicknesses. A quantitative estimate of multiple-scattering effects is thus not easy. For example, in our case, the Lambert–Beer law predicts a maximum relative intensity imbalance of approximately 23% at low intensity, which is not negligible. However, our experimental results strongly suggest that multiple-scattering velocity inhomogeneous broadening is small. Indeed, as  $s_0$  is increased, the optical thickness decreases because the scattering cross section is reduced. The compression force is thus decreased and cannot explain the strong increase of  $\sigma_v$  versus  $s_0$  evidenced in Fig. 4. Furthermore, multiple scattering induces some correlations between position

and velocity that should alter the cloud ballistic expansion. This has not been observed in Fig. 2. As an ultimate test, we have changed the number of atoms in the MOT by a factor of 3 without detecting any modification of  $\sigma_v$ .

### 3. COOLING WITH INTENSITY IMBALANCE

We analyze in this section how spatial stationary transverse intensity fluctuations can modify the Doppler cooling predictions in a quantitative way. Starting from the analytical expression of the average force in 1D molasses, we take into account these spatial intensity fluctuations, and we derive analytical results in two limiting cases, namely, when cooling is achieved before intensity fluctuates and in the opposite case. This analytical model neglects the photon noise encapsulated in the Langevin force  $F_v$ , leading to a nonzero Doppler temperature. However, for a quantitative comparison with experimental data, we have developed a MC simulation that fully takes into account all fluctuating mechanisms (molasses intensity fluctuations and photon noise). These results will be detailed in Subsections 3.C and 3.D.

#### A. Origin of Spatial Intensity Imbalance

In the standard Doppler theory, the molasses beams are described as perfect plane waves. In real experiments, however, the beams have a Gaussian-shaped transverse profile. Usually one can ignore the transverse dimensions of the beams because they are generally much larger than the MOT size. Nevertheless, the transverse intensity profiles are not defect-free ideal Gaussian profiles. Indeed, even starting from diffraction-limited laser beams, imperfections of optics elements (dust, aberrations, etc.) induce scattering that generates an intensity speckle. Of course, in well-controlled experiments, this speckle pattern remains relatively small compared with the average beam intensity, but those two fields add coherently. In our experiment, we have measured the laser beam's spatial transverse fluctuations by placing a CCD camera at the approximative position of the MOT. Subtracting the ideal Gaussian profile, we have computed the intensity fluctuations' histogram (see Fig. 5). We found a Gaussian histogram with a relative standard deviation (with respect to the average intensity) in the range 10%–20%.

The 1D molasses is created by two contrapropagating beams issued from the same source. However, the speckle intensity generated by the optics imperfections in each arm is independent. It is thus reasonable to consider, at each transverse position in the beam profile, the intensities  $I_i$  ( $i = 1, 2$ ) of the two molasses beams to be random independent Gaussian variables. Noting by  $s_i$  the corresponding on-resonance saturation parameters, we assume the probability distribution  $\mathcal{P}(s_i)$  to be the same for the two beams. Hence the (common) first two moments, at each transverse position, are  $\langle s_i \rangle = s_0$  and  $\sigma_s^2 = \langle (s_i - s_0)^2 \rangle$  ( $i = 1, 2$ ). In the following we will characterize the molasses intensity fluctuations by the ratio  $r_s = \sigma_s / 2s_0$ . From experimental data, we have  $r_s$  in the range 5%–10%. Another important feature is the transverse spatial correlation function (assumed to be the same for each beam), namely,  $\mathcal{C}(\mathbf{r}) = \langle s_i(\mathbf{r}') s_i(\mathbf{r}' + \mathbf{r}) \rangle$  ( $i = 1, 2$ ). The characteristic decay

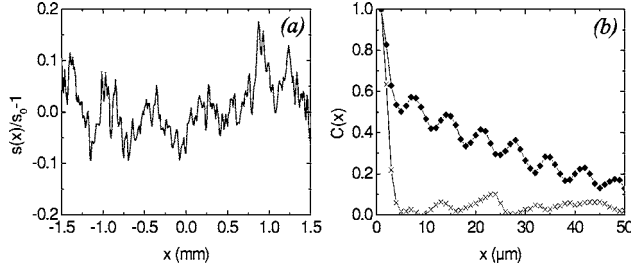


Fig. 5. (a) Typical relative intensity fluctuations of a laser beam once the smooth Gaussian profile is removed. The typical intensity dispersion is roughly 10% of the total signal. (b) The spatial fluctuations correlation function  $C(x)$  versus a transverse coordinate. The transverse distance at which this correlation function vanishes defines the correlation length  $\xi_s$ . Experimentally, we found  $\xi_s \approx 30 \mu\text{m}$  (diamonds). The oscillation on top of the decay is due to the interference generated by the front window of the CCD camera. The fast decrease observed at short distances is also present when the laser is off (crosses). This fast decrease is thus due to the uncorrelated noise on the CCD camera and corresponds to the pixel size.

length of  $C(\mathbf{r})$  defines the transverse correlation length  $\xi_s$ . Strictly speaking, because of diffraction effects,  $\xi_s$  cannot be zero. We have experimentally found  $\xi_s$  to be of the order of few tenths of micrometers ( $\xi_s = 30 \mu\text{m}$  for the example shown in Fig. 5).

## B. Analytical Model

For a  $0 \rightarrow 1$  transition in the lin||lin configuration, atoms are modeled by a two-level system involving the same Zeeman states for each molasses beam. The two beams have the same red-detuned frequency ( $\delta < 0$ ), opposite wave vector  $\mathbf{k}$ , but have locally different saturations that fluctuate independently across the transverse profile of the beams but with the same correlation length  $\xi_s$ . The mean local radiation pressure force experienced by a single atom, with longitudinal velocity  $v$ , takes the simple following form:

$$F = m \frac{v_R \Gamma}{2} \left[ \frac{s_1}{1 + s_1 + s_2 + (\Delta - 2kv/\Gamma)^2} - \frac{s_2}{1 + s_1 + s_2 + (\Delta + 2kv/\Gamma)^2} \right] \quad (2)$$

$$\approx m \frac{v_R \Gamma}{2} \left[ \frac{s_1}{1 + 2s_0 + (\Delta - 2kv/\Gamma)^2} - \frac{s_2}{1 + 2s_0 + (\Delta + 2kv/\Gamma)^2} \right], \quad (3)$$

where  $v_R = \hbar k/m$  is the recoil velocity ( $\approx 6 \text{ mm/s}$  for Sr). We have here assumed that the mechanical actions of the two laser beams can be added independently, only considering the total saturation of the optical transition to be  $(s_1 + s_2)$ . We have furthermore replaced  $(s_1 + s_2)$  with  $2s_0$  in the denominator. A more careful analysis, along the lines given below, shows that this is indeed valid with our experimental parameters.

Near the steady state, the Doppler broadening becomes negligible,  $kv \ll (\Gamma, \delta)$ , and the force can be safely approximated by

$$F \approx -m(s_1 + s_2)\gamma_v v + m(s_1 - s_2)a \quad (4)$$

$$\approx -2ms_0\gamma_v v + m(s_1 - s_2)a. \quad (5)$$

Defining the recoil angular frequency  $\omega_R = 2\pi\nu_R = \hbar k^2/2m$  ( $\nu_R \approx 10.6 \text{ kHz}$  for Sr), we have

$$\gamma_v = \omega_R \frac{4|\Delta|}{(1 + \Delta^2 + 2s_0)^2}, \quad a = \frac{v_R \Gamma}{2} \frac{1}{1 + \Delta^2 + 2s_0}. \quad (6)$$

The friction force is given by the term proportional to  $v$  and gives rise to a mean damping time:

$$\tau_v = (2s_0\gamma_v)^{-1}. \quad (7)$$

Consider now an atom moving across the molasses beams with transverse velocity  $v_\perp$ . This velocity is unaffected by the longitudinal cooling. So, as the atom flies across the beam, it may experience induced temporal molasses intensity fluctuations. The induced correlation time of these fluctuations is simply

$$\tau_s = \xi_s/v_\perp. \quad (8)$$

Thus we have two competing dynamical processes, the cooling one with characteristic time  $\tau_v$  and the intensity random (induced) temporal variations with correlation time  $\tau_s$ . The global velocity dynamics can be easily analyzed when these time scales are well separated.

### 1. Regime $\tau_v \ll \tau_s$

For atoms fulfilling this condition, the damping process is completed before intensities fluctuate. Then the constant force and the friction coefficient in expression (4) can be considered time independent. Atoms thus behave as if  $v_\perp$  were zero. However, because  $\xi_s$  is much shorter than the cloud size, each atom experiences randomly fixed distributed intensity imbalances and, in turn, a random constant force. The random stationary velocity is  $v_\infty = a\tau_v(s_1 - s_2)$ . It is Gaussian distributed with zero mean and dispersion:

$$\sigma_\infty = \sqrt{2}a\tau_v\sigma_s = \sqrt{2} \frac{\Gamma}{k} \frac{1 + |\Delta|^2 + 2s_0}{4|\Delta|} r_s. \quad (9)$$

To find the final velocity distribution, one has to incorporate the photon noise force  $F_v$ . As the photon noise and intensity fluctuations are independent, the total velocity variance is the sum of the Doppler and intensity variances  $\sigma_v^2 = \sigma_D^2 + \sigma_\infty^2$ . In this regime, intensity fluctuations thus give rise to an extra-heating mechanism inducing an inhomogeneous broadening of the Doppler velocity distribution. At  $\Delta = -1$ ,  $s_0$  small, and  $r_s = 9\%$ , one gets  $\sigma_\infty \approx 0.94 \text{ m/s}$  and  $\sigma_v \approx 0.97 \text{ m/s}$ .

### 2. Regime $\tau_v \gg \tau_s$

In this regime, the molasses intensities fluctuate wildly before the atom reaches its stationary state. Thus they cannot be treated as time-independent quantities. They can, however, be treated as independent Markovian (short-memory) processes. From expression (4) of the total force, we derive the following master equation for the velocity distribution  $P_i(v)$ <sup>22</sup> (details will be given elsewhere):

$$P(v, t + \tau_s) = \int ds_1 ds_2 dv' \mathcal{P}(s_1) \mathcal{P}(s_2) P(v', t) \delta\left(v - v' - \frac{F}{m} \tau_s\right). \quad (10)$$

In this equation, at each time step  $\tau_s$ , the saturations  $s_1$  and  $s_2$  take on new values uncorrelated with the previous ones.

One should note that we have kept here both the additive noise, given by the  $(s_1 - s_2)$  term, and the multiplicative noise, given by the  $(s_1 + s_2)v$  term. This last term had been replaced by  $2s_0v$  in our previous analysis [expression (5) of the force]. In the limit of small velocity changes at the elementary time scale  $\tau_s$ , one can derive from Eq. (10) a Fokker–Planck-type equation (see Appendix A):

$$\frac{\partial P(v, t)}{\partial t} = \frac{1}{\tau_v} \frac{\partial}{\partial v} [vP(v, t)] + \frac{\partial^2}{\partial v^2} [D(v)P(v, t)]. \quad (11)$$

Defining  $D_\infty = \sigma_\infty^2 / 2\tau_v$ , we find that the velocity-dependent diffusion constant has the following expression:

$$D(v) = D_\infty [1 + (1 + 2r_s^2)(v/\sigma_\infty)^2] \frac{\tau_s}{\tau_v} \approx D_\infty [1 + (v/\sigma_\infty)^2] \frac{\tau_s}{\tau_v} \quad (12)$$

in that generally  $2r_s^2 \ll 1$ . This velocity dependence originates from the multiplicative noise and leads to abnormal diffusion. The stationary velocity distribution  $P_0$  is then easily found to take the following form ( $\mathcal{N}$  is a normalization constant):

$$P_0(v) \approx \mathcal{N} [1 + (v/\sigma_\infty)^2]^{-(1+\eta)}, \quad (13)$$

where  $\eta = \tau_v / \tau_s \gg 1$ . The full width at half-maximum of this distribution is

$$\Gamma_v = 2\sqrt{\ln 2} \sqrt{\frac{\tau_s}{\tau_v}} \sigma_\infty \ll \sigma_\infty. \quad (14)$$

As can be easily checked,  $D(v) \approx D_\infty \tau_s / \tau_v$  for  $v \sim \Gamma_v$ . Hence the impact of abnormal diffusion is in fact negligible when  $\tau_v \gg \tau_s$ , and the velocity distribution is close to a Gaussian with velocity dispersion

$$\sigma_v \sim \sqrt{\frac{\tau_s}{\tau_v}} \sigma_\infty \ll \sigma_\infty, \quad (15)$$

which is much narrower than the velocity dispersion found in the long correlation limit [Eq. (9)] by the factor  $\sqrt{\tau_s / \tau_v}$ .

Figure 6 shows  $\sigma_v$  as a function of  $r_s$  in the long and short correlation time limits ( $\Delta = -1, s_0 \ll 1$ ). When  $r_s \rightarrow 0$ ,  $\sigma_v$  goes to zero in both limits. This does not mean that the temperature goes to zero in experiments. Indeed, in the previous discussion we have discarded the photon noise at the physical origin of the bare Doppler theory. Its contribution at low saturation is given by the dotted line in Fig. 6. We can see that the noise induced by long correlation times starts to dominate at  $r_s > 2.5\%$ , a fairly small value. Hence, to achieve cooling up to the Doppler limit at  $\Delta = -1$ , one has to minimize the ratio  $\tau_c / \tau_v$  for a fixed value of  $r_s$ . This can be done in different ways. First, one can decrease the laser intensity to increase  $\tau_v$ . Sec-

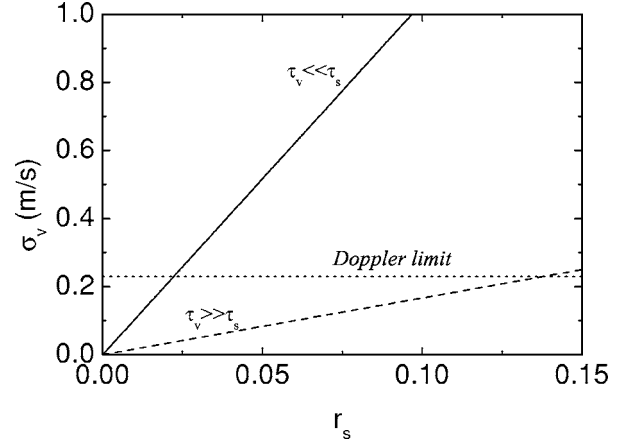


Fig. 6. Velocity dispersion  $\sigma_v$  for the long (solid line) and short (dashed line) correlation time limits as a function of the relative fluctuation of the intensity  $r_s = \sigma_c / 2s_0$ . In the short correlation time limit,  $\tau_s = 30 \mu\text{s}$ . The dotted line corresponds to the Doppler limit at low saturation and  $\Delta = -1$  (see text).

ond, one can decrease  $\tau_s$ . As shown by Eq. (8), this can be achieved either by avoiding large transverse intensity defects in the laser profiles to decrease the correlation length  $\xi_s$  or by increasing  $v_\perp$ . This, indeed, has been observed in an atomic beam experiment<sup>23</sup> in which temperatures close to the Doppler limit had been found along one transverse dimension.

In a MOT, if the fluctuations of the transverse intensities are not the same for all three dimensions, the temperature is expected to be anisotropic. Moreover, coupling mechanisms occur between the cooling dimensions. Thus high velocity dispersion along one dimension tends to reduce the temperature in the orthogonal plane. In our 1D molasses, the transverse velocity is fixed by the initial MOT sequence, and  $\tau_s / \tau_v$  is usually bigger than 1. As we will see in Subsection 3.D, this means that transverse intensity fluctuations are the major heating mechanism.

### C. Monte Carlo Simulations

To quantitatively test our theory, and not relying on questionable approximations, we have developed a MC simulation. This MC simulation fully takes into account the photon noise leading to the Doppler cooling limit, saturation of the transitions, and the transverse intensity fluctuations discussed so far, i.e., with arbitrary correlation time  $\tau_s$  and saturation dispersion  $\sigma_s$ .

The shortest time scale in the MC calculation is given by the excited-state lifetime  $\tau_e = 1/\Gamma$ . To mimic the transverse flight of atoms, the molasses saturation fluctuations  $\delta s_i = (s_i - s_0)$  ( $i = 1, 2$ ) become time-dependent parameters and evolve according to the damped random-path discrete equation ( $n$  labels the number of time steps  $\tau_e$ )

$$\delta s_i(n+1) = (1 - \rho) \delta s_i(n) + R_n, \quad (16)$$

with  $\rho \ll 1$ . The first term in this equation is the friction term, relaxing saturation to its stationary value  $s_0$ , and the last term is a random variable, with zero mean value, uniformly distributed over the range  $[-\epsilon/2, \epsilon/2]$ . A simple calculation shows that  $\langle R_n^2 \rangle = \epsilon^2 / 12$ . We further assume that the  $R_n$ 's are decorrelated. The continuous limit of Eq. (16) is

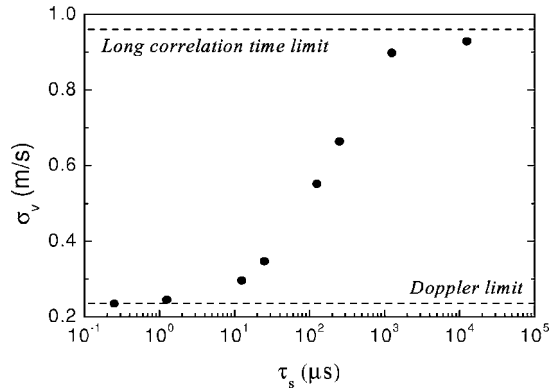


Fig. 7. Final velocity dispersion  $\sigma_v$  as a function of the correlation time  $\tau_s$  (circles). Both the transverse and the longitudinal velocity dispersions are equal to  $\Delta v = 0.8$  m/s. The mean saturation of each beam is  $s_0 = 0.04$ , and the saturation fluctuation parameter is  $r_s = 9\%$ . The upper dashed line represents the long correlation time limit, and the lower one represents the Doppler cooling limit (see text).

$$\frac{d\delta s_i}{dt} + \frac{\rho}{\tau_e} \delta s_i = R(t). \quad (17)$$

As the correlation time  $\tau_s$  should correspond to the damping time of this equation, we see that  $\rho = \tau_e / \tau_s$ . Thus fixing  $\tau_s$  fixes  $\rho$  in Eq. (16). The last term of Eq. (17) is a delta-correlated Langevin term with zero mean. Its time-correlation function is  $\langle R(t')R(t) \rangle = 2D\delta(t-t')$ , where it is easily shown that  $D = \epsilon^2 / 24\tau_e$ . The fluctuation-dissipation theorem then dictates  $\sigma_s^2 = D\tau_s$ , leading to

$$\epsilon = 2\sqrt{6\rho\sigma_s}. \quad (18)$$

One can find this last result more elegantly by squaring Eq. (16) and averaging over the probability distribution of  $R_n$ . Hence experimental determination (or convenient choice) of the macroscopic ingredients  $\tau_s$  and  $\sigma_s$  fixes, in principle, the microscopic ingredients  $\epsilon$  and  $\rho$  in Eq. (16).

Figure 7 shows the obtained final velocity dispersion  $\sigma_v$  as a function of  $\tau_s / \tau_v$  for  $s_0 = 0.04$  and  $r_s = 9\%$ . The velocity damping time, calculated with Eq. (7), is  $\tau_v = 200 \mu\text{s}$ . As expected,  $\sigma_v$  is higher for long correlation times  $\tau_s \gg \tau_v$ . When  $\tau_s \sim \tau_v$ ,  $\sigma_v$  is sensitive to  $\tau_s$ . At lower values  $\tau_s \ll \tau_v$ ,  $\sigma_v$  is minimum and, for these parameters, reaches the Doppler limit. The final distributions (not shown here) are quasi Gaussian, even at small  $\tau_s$ .

#### D. Quantitative Comparison with Experimental Data

We have shown in Subsection 2.C that the measured velocity dispersions were always larger than the Doppler theory predictions. We now compare our experimental data with the results of our previous MC simulation. To stick as close as possible to the experiments, we also take into account the transverse velocity distribution (a centered Gaussian with dispersion  $\Delta v_\perp \approx 0.8$  m/s) in the MC simulation.

In Fig. 3 the solid curve corresponds to the MC simulation performed at  $r_s = 9\%$  and  $\xi_s = 60 \mu\text{m}$ . These quantities are fit parameters in the MC simulation but remain in the range of the measured ones (see Subsection 3.A). As one can see, the agreement with experimental points is now good, providing a clear understanding of the physics at

work in the experiment. Coming back to Eqs. (6), close to resonance, the friction term decreases while the intensity imbalance term increases. Hence, the mismatch between experiment and Doppler theory is maximal.

Again, an excellent agreement between MC simulation (solid curve) and data is found in Fig. 4. To properly understand these results, one has to note that the crossover region between the long and short correlation time limits is given by  $\tau_s = \tau_v$ , or, equivalently, by  $s_0 = v_\perp / 2\gamma_v \xi_s \sim 0.1$ . TOF measurements before the molasses sequence have shown that  $v_\perp \approx 0.8$  m/s, whereas  $\xi_s$  is the chosen MC parameter. This is exactly what is seen in Fig. 4, and the Doppler theory is recovered when  $s_0 \rightarrow 0$ . However, this short correlation time limit ( $\tau_s \ll \tau_v$ ) was not experimentally accessible because the 1D cooling duration sequence was not long enough to reach the steady state. This is why most of the data points correspond to the long correlation time limit ( $\tau_s \gg \tau_v$ ) and can be compared with Eq. (9). This is done in Fig. 4, where the dashed line corresponds to the prediction given by Eq. (9). The general behavior is correct, indicating that saturation of the atomic transition indeed plays a significant role. However the prediction [Eq. (9)] is a little bit too large. This is not surprising in that, for the explored range of parameters, some atoms will always have sufficiently high transverse velocities to fulfill the short-correlation-time criterion, both in the experiment and in the MC simulation. As a consequence, the velocity dispersion  $\sigma_v$  will be reduced. In other words, Eq. (9) corresponds to a zero-transverse velocity case, giving overestimated predictions.

Figure 8 shows the longitudinal spatial distribution obtained for the longest ballistic time at  $\Delta = -1$  and  $s_0 = 0.08$ . It is two times broader than the initial spatial distribution and essentially proportional to the velocity distribution. We can then try to compare it with the velocity distribution obtained with the MC simulation (solid curve). We have also plotted the Gaussian distribution expected from standard Doppler theory (dashed curve). The actual non-Gaussian shape of the MC distribution is explained by the transverse velocity dispersion ( $\Delta v_\perp \approx 0.8$  m/s). For each fixed transverse velocity, the distribution is quasi Gaussian with a width depending on  $v_\perp$  (see Fig. 6 and discussions in Subsection 3.B). For this simple reason, summing over the transverse velocity dis-

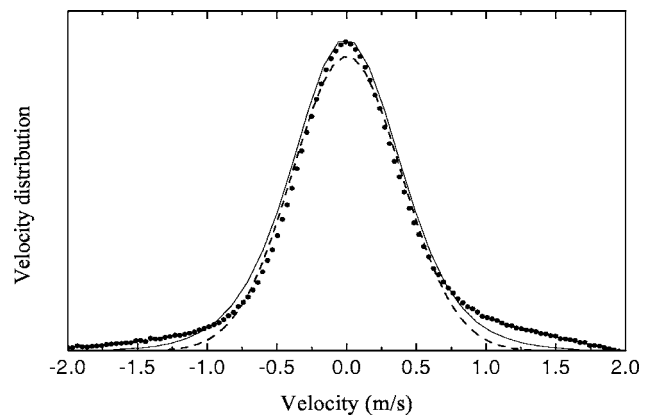


Fig. 8. Velocity distribution obtained at  $s_0 = 0.08$  and  $\Delta = -1$ . Circles, experiment; dashed curve, Gaussian fit; solid curve, MC simulation with  $r_s = 7.5\%$  and  $\tau_s = 20 \mu\text{s}$  (see text).

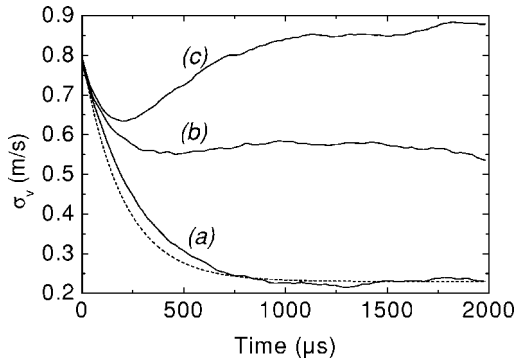


Fig. 9. MC simulations of the time evolution of the velocity dispersion  $\sigma_v$  for three characteristic correlation times: (a) short correlation time ( $\tau_s = 1.25 \mu\text{s}$ ), (b) intermediate correlation time ( $\tau_s = 125 \mu\text{s}$ ), and (c) long correlation time ( $\tau_s = 1250 \mu\text{s}$ ). The transverse velocity dispersion is  $\Delta v_{\perp} = 0.8 \text{ m/s}$ , the mean saturation per beam is  $s_0 = 0.04$ , and the saturation fluctuation parameter is  $r_s = 9\%$ . The dashed exponential decay is the bare Doppler prediction (see text).

tribution leads to a non-Gaussian distribution. The non-Gaussian shape of the MC simulation matches the experimental distribution better than the Gaussian one.

As a conclusion of this section, we again stress that we have quantitatively explained both the behavior of the velocity dispersion  $\sigma_v$  as a function of laser detuning and intensity and the observed non-Gaussian distributions. This puts strong evidence on the fundamental role played by molasses intensity defects in the cooling process.

#### 4. COOLING DYNAMICS

Figure 9 shows the time evolution of  $\sigma_v$  for three different values of  $\tau_c$  corresponding to the short, intermediate, and long correlation time limits. When  $\tau_s$  is short (or, equivalently,  $v_{\perp}$  is large), the corresponding curve (a) displays an exponential-type behavior decaying to the Doppler steady-state value. This curve is in agreement with the dashed-curve Doppler prediction. When  $\tau_s$  is long (or, equivalently,  $v_{\perp}$  is small), the dynamics evidenced by curve (c) is more complex. First,  $\sigma_v$  reaches a minimum value within a time scale corresponding to the damping time  $\tau_v$ . Then  $\sigma_v$  increases again and reaches the steady-state value  $\sigma_{\infty}$  predicted by Eq. (9). When the mean velocity and the local intensity imbalance are uncorrelated in the initial state, then this long-correlation-time behavior is generic and does not depend anymore on the initial state. Because the intensity correlation length  $\xi_s$  is large, the heating mechanism also takes some time to build up, and the initial velocity distribution starts first to shrink. This is easily explained by one's considering the dynamics induced by expression (4) for times shorter than  $\tau_s$ , where transverse intensity fluctuations are dynamically frozen. After a proper averaging over intensity fluctuations, the following analytic expression for  $\sigma_v(t)$  is derived:

$$\sigma_v(t)^2 = (\Delta v^2 + \sigma_{\infty}^2) \exp(-2t/\tau_v) + \sigma_{\infty}^2 [1 - \exp(-t/\tau_v)], \quad (19)$$

where  $\Delta v$  corresponds to the initial longitudinal velocity dispersion. The small time expansion  $t \ll \tau_v$  of this equation gives

$$\sigma_v(t) \approx \Delta v(1 - t/\tau_v), \quad (20)$$

clearly evidencing the velocity spread narrowing at small times. We have experimentally tested this specific behavior. Once the MOT is loaded, we have switched off the cooling laser beams within a time window of variable duration  $\tau_{\text{dark}}$ . This dark sequence must be long enough to allow atoms to travel over transverse distances larger than the correlation length  $\xi_s$  of intensity fluctuations. Then, once the cooling lasers are switched on again, any correlation between the mean atomic velocity and the local intensity imbalance is wiped out. We should thus observe the behavior predicted by curve (c) in Fig. 9. The velocity dispersion  $\sigma_v$  is measured after a time  $\tau$  by the TOF technique (see section 2). In Fig. 10(a), we plot  $\sigma_v$  as a function of  $\tau$  after a dark period  $\tau_{\text{dark}} = 0.5 \text{ ms}$ . We reproduce nicely the corresponding theoretical prediction. First, we observe a decrease of  $\sigma_v$  followed by an increase, up to the final value (which is here the same as the initial value). We also checked that the dark period has to be long enough, as evidenced in Fig. 10(b). When  $\tau_{\text{dark}}$  is short enough (less than 1 ms), decorrelation between the mean atomic velocity and local intensity imbalances is not completed. When  $\tau_{\text{dark}}$  is long enough (larger than 1 ms), complete decorrelation is achieved, and the dark period no longer plays any role in the cooling dynamics.

For practical reasons, these experiments were done with the MOT (i.e. on an three-dimensional cooling configuration in the presence of the magnetic field gradient), whereas the MC simulations were done for a 1D cooling scheme. This major difference does not allow for a quantitative comparison between theory and experiment. However, the qualitative agreement is pretty good. This result suggests that the dominant extra-heating mechanism in a MOT is the same as in 1D molasses.

Because the velocity distribution always starts with a compression period, one could imagine a cooling strategy implementing suitable repetitions of dark time windows to achieve Doppler-limited cooling. This simple idea, however, is not easy to handle because complete decorrelation between initial atomic velocities and intensity imbalances during these dark windows is requested. As the cloud cools down, the duration of the subsequent dark periods has to be increased accordingly to maintain this decorrelation. Unfortunately, as soon as the cooling time becomes long, spurious effects, such as large cloud expansions, then have time to set in.

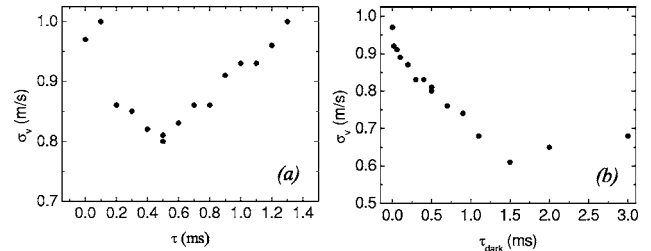


Fig. 10. (a) Time evolution of the velocity dispersion  $\sigma_v$  after a dark time window of duration  $\tau_{\text{dark}} = 0.5 \text{ ms}$ ; (b) MOT velocity dispersion  $\sigma_v$  as a function of the dark-window duration. The dark window starts 0.5 ms after the beginning of the cooling sequence (see text).

## 5. CONCLUSIONS

We have evidenced in this paper the important role played by transverse spatial intensity fluctuations in 1D laser cooling of zero-spin ground-state atoms in which no Sisyphus cooling can occur. For intensity-imbalanced molasses beams, the total radiation pressure force decomposes, at small velocities, into a friction force and a constant force. The latter is at the root of an additional heating mechanism. These two forces essentially depend linearly on the molasses intensities. In the presence of sub-Doppler cooling mechanisms, the friction term becomes intensity independent, whereas the constant force remains proportional to the intensity.<sup>6,24,25</sup> Hence, with sub-Doppler cooling, the effect of intensity imbalances can be arbitrarily small and, in turn, does not play any significant role. This is completely different for Doppler cooling, in which this effect remains dominant in most experimental cases.

The cooling steady state reached by the atoms depends sensitively on the ratio  $\zeta$  between the correlation length of transverse intensity fluctuations and the transverse distance traveled by the atoms before reaching the steady state. For small  $\zeta$ , the transverse fluctuations can be modeled by a Langevin force inducing an additional heating mechanism. For large  $\zeta$ , the equilibrium state is reached at frozen molasses intensities. Atoms at different transverse positions then probe all possible intensity imbalances. This averaging procedure mainly affects the final atomic velocity and induces an inhomogeneous broadening of the Doppler velocity distribution. The impact on the final temperature is more severe than in the small  $\zeta$  regime. This is evidenced by our experimental data, which mostly lie in the large  $\zeta$  regime. It is, however, possible, in principle, to reach the small  $\zeta$  regime by appropriately reducing the intensities of the cooling beams and get final temperatures closer to the Doppler limit.

The cooling dynamics also exhibits an unusual behavior in the large  $\zeta$  regime: The atoms are first cooled down before being heated up. This specific feature is also found in our experiments, thus confirming the central role of transverse intensity fluctuations in Doppler cooling.

## ACKNOWLEDGMENTS

This research is financially supported by the Centre National de la Recherche Scientifique and the Bureau National de Métrologie contract 03 3 005.

D. Wilkowski, the corresponding author, can be reached by e-mail at david.wilkowski@inln.cnrs.fr.

## APPENDIX A: DERIVATION OF THE MASTER EQUATION

One obtains the Fokker–Planck-type equation (Eq. (11)) by starting with the master equation (10):

$$P(v, t + \tau_s) = \int ds_1 ds_2 dv' \mathcal{P}(s_1) \mathcal{P}(s_2) P(v', t) \delta \left[ v - v' - \frac{F(s_1, s_2, v')}{m} \tau_s \right]. \quad (\text{A1})$$

By Fourier transforming this equation with respect to  $v$ , we get

$$\tilde{P}(q, t + \tau_s) = \frac{1}{\sqrt{2\pi}} \int ds_1 ds_2 dv' \mathcal{P}(s_1) \mathcal{P}(s_2) P(v', t) \times \exp \left\{ -iq \left[ v' + \frac{F(s_1, s_2, v')}{m} \tau_s \right] \right\}. \quad (\text{A2})$$

We now plug expression (4) of the force in this equation to find

$$\tilde{P}(q, t + \tau_s) = \frac{1}{\sqrt{2\pi}} \int dv' \tilde{P}[q\tau_s(a - \gamma_v v')] \tilde{P}^* \times [q\tau_s(a + \gamma_v v')] P(v', t) \exp(-iqv'), \quad (\text{A3})$$

where the asterisk denotes complex conjugation and where

$$\tilde{P}(u) = \int ds \mathcal{P}(s) \exp(-ius) \quad (\text{A4})$$

is proportional to the Fourier transform of the molasses saturation distribution  $\mathcal{P}$ . As discussed in Subsection 3.A, the distribution  $\mathcal{P}$  is a Gaussian with mean  $s_0$  and dispersion  $\sigma_s$ . A Taylor expansion of Eq. (A3) up to second order in  $\tau_s$  then leads to

$$\tau_v \frac{\partial \tilde{P}(q, t)}{\partial t} \simeq \frac{1}{\sqrt{2\pi}} \int dv' \left\{ iqv' - q^2 \frac{\tau_s}{2\tau_v} \left[ v'^2 (1 + 2r_s^2) + 2r_s^2 \frac{a^2}{\gamma_v^2} \right] \right\} P(v', t) \exp(-iqv'). \quad (\text{A5})$$

An inverse Fourier transform then gives Eq. (11) once we note that  $\sigma_\infty = \sqrt{2} r_s a / \gamma_v$  according to Eq. (9).

## REFERENCES

1. S. Haroche, "Fundamental systems in quantum optics," *Les Houches LIII*, J. Dalibard, J. M. Raimond, and J. Zinn-Justin, eds. (North-Holland, 1992).
2. M. H. Anderson, J. R. Ensher, M. R. Matthews, C. E. Wieman, and E. A. Cornell, "Observation of Bose–Einstein condensation in a dilute atomic vapor," *Science* **269**, 198–201 (1995).
3. K. Davis, M. O. Mewes, M. R. Andrews, N. J. van Druten, D. S. Durfee, D. M. Kurn, and W. Ketterle, "Bose–Einstein condensation in a gas of sodium atoms," *Phys. Rev. Lett.* **75**, 3969–3973 (1995).
4. T. W. Hansch and A. L. Schawlow, "Cooling of gases by laser radiation," *Opt. Commun.* 0030-4018 **13**, 68–69 (1975).
5. D. J. Wineland and H. Dehmelt, "Proposed  $10^{14} \delta\nu/\nu$  laser fluorescence spectroscopy on  $\text{Ti}^+$  mono-ion oscillator III (side band cooling)," *Bull. Am. Phys. Soc.* **20**, 637 (1975).
6. P. Lett, W. Phillips, S. Rolston, C. Tanner, R. Watts, and C. Westbrook, "Optical molasses," *J. Opt. Soc. Am. B* **6**, 2084–2107 (1989).
7. J. Dalibard and C. Cohen-Tannoudji, "Laser cooling below the Doppler limit by polarization gradients: simple theoretical models," *J. Opt. Soc. Am. B* **6**, 2023–2045 (1989).
8. P. J. Ungar, D. S. Weiss, E. Riis, and S. Chu, "Optical molasses and multilevel atoms: theory," *J. Opt. Soc. Am. B* **6**, 2058–2071 (1989).
9. C. W. Oates, F. Bondu, and L. Hollberg, "A diode-laser optical frequency standard based on laser-cooled Ca atoms: sub-kilohertz spectroscopy by optical shelving detection," *Eur. Phys. J. D* **7**, 449–460 (1999).
10. F. Loo, A. Bruschi, S. Sauge, M. Allegrini, E. Arimondo, N.

- Andersen, and J. Thomsen, "Investigations of a two-level atom in a magneto-optical trap using magnesium," *J. Opt. B* **6**, 81–85 (2004).
11. X. Xu, T. Loftus, M. Smith, J. Hall, A. Gallagher, and J. Ye, "Dynamics in a two-level atom magneto-optical trap," *Phys. Rev. A* **66**, 011401 (2002)
  12. X. Xu, T. Loftus, J. Hall, and J. Ye, "Cooling and trapping of atomic strontium," *J. Opt. Soc. Am. B* **20**, 968–976 (2003).
  13. T. H. Yoon, Korean Research Institute of Standards and Science, Yuseong Daejeon 305-600, Korea. (personal communication, 2004).
  14. J. Piilo, E. Lundh, and K.-A. Suominen, "Radiative collisional heating at the Doppler limit for laser-cooled magnesium atoms," *Phys. Rev. A* **70**, 013410 (2004).
  15. M. Drewsen, P. Laurent, A. Nadir, G. Santerelli, A. Clairon, Y. Castin, D. Grison, and C. Salomon, "Investigation of sub-Doppler cooling effects in a cesium magneto-optical trap," *Appl. Phys. B* **59**, 283–298 (1994).
  16. C. Cooper, G. Hillenbrad, J. Rink, C. Townsend, K. Zetie, and C. Foot, "The temperature of atoms in magneto-optical trap," *Europhys. Lett.* **28**, 397 (1994).
  17. D. S. Weiss, E. Riis, Y. Shery, P. J. Ungar, and S. Chu, "Optical molasses and multilevel atoms: experiment," *J. Opt. Soc. Am. B* **6**, 2072–2083 (1989).
  18. J. Dalibard and C. Cohen-Tannoudji, "Atomic motion in laser light: connection between semiclassical and quantum descriptions," *J. Phys. B* **18**, 1661–1683 (1985).
  19. B. Klappauf, Y. Bidel, D. Wilkowski, T. Chanelière, and R. Kaiser, "Detailed study of an efficient blue laser source by second-harmonic generation in a semimonolithic cavity for the cooling of strontium atoms," *Appl. Opt.* **43**, 2510–2527 (2004).
  20. J. Gordon and A. Ashkin, "Motion of atoms in a radiation trap," *Phys. Rev. A* **21**, 1606–1617 (1980).
  21. D. W. Sesko, T. G. Walker, and C. E. Wieman, "Behavior of neutral atoms in a spontaneous force trap," *J. Opt. Soc. Am. B* **8**, 946–958 (1991).
  22. N. G. Van Kampen, *Stochastic Progresses in Physics and Chemistry* (North-Holland, Amsterdam, 1981).
  23. A. Witte, Th. Kisters, F. Riehle, and J. Helmcke, "Laser cooling and deflection of a calcium atomic beam," *J. Opt. Soc. Am. B* **9**, 1030–1037 (1992).
  24. A. Steane, M. Chowdhury, and C. Foot, "Radiation force in the magneto-optical trap," *J. Opt. Soc. Am. B* **9**, 2142–2158 (1992).
  25. J. Werner and H. Wallis, "Laser cooling by  $\sigma^+ - \sigma^-$  circularly polarized beams of unequal intensities," *J. Phys. B* **26**, 3063–3080 (1993).